Graphdiyne facilitates photocatalytic CO_2 hydrogenation into C_{2+} hydrocarbons

Wenjuan Li, Yipin Zhang, Yuhua Wang, Weiguang Ran, Qinhui Guan, Wencai Yi, Lulu Zhang, Dapeng Zhang, Na Li, Tingjiang Yan [*]

Key Laboratory of Catalytic Conversion and Clean Energy in Universities of Shandong Province, School of Chemistry and Chemical Engineering, Qufu Normal University, PR China

ARTICLE INFO

ABSTRACT

Graphdiyne (GDY) is firstly introduced to the gaseous photocatalytic CO_2 hydrogenation system for C_{2+} production, in which a GDY-modified In_2O_3 nanocomposite (denoted as GDY-IO) is fabricated by simple electrostatic attraction and thermal treatment routes. GDY-IO delivers much higher performance for CO_2 hydrogenation compared to that of pristine In_2O_3, reflecting by the significantly improved C_1 (CO and CH_4) yield and the newly formed C_{2+} hydrocarbons (C_2H_4, C_2H_6, C_3H_6, and C_3H_8). The introduction of GDY promotes the transport of photogenerated holes from In_2O_3 to GDY and suppresses the recombination of photogenerated carriers, thereby gathering abundant electrons to participate in the CO_2 hydrogenation reaction. GDY-IO interface may stabilize the key HOCH* intermediate and significantly reduce the kinetics barrier to avail CH* formation, tuning the subsequent hydrogenation and C-C coupling into thermodynamically favorable exothermic processes. This research develops a new avenue for synthesis of high value-added chemical fuels from greenhouse gases by graphdiyne-based photocatalysis.

1. Introduction

Since the overexploitation and utilization of fossil energy bring huge CO_2 emissions, the way to promote the revolution of energy production and consumption with the purpose of building a low-carbon, safe and efficient energy system, has been drawn increasing attention at present [1–5]. Using solar energy to generate chemical fuels especially high value-added multi-carbon (C_{2+}) products from CO_2 has the potential to reduce CO_2 emissions and facilitates the sustainable development of clean energy [3–8].

Photocatalytic CO_2 reduction is a multi-electron coupled proton transfer process, which needs sufficient photoinduced electrons to participate in the photocatalytic reduction process [9]. The preparation of desirable C_{2+} compounds from CO_2 requires overcoming the activation of C=O bonds and the coupling of C-C bonds kinetically [10]. Although many semiconductor catalysts such as TiO_2 [11], COFs [12], Cs_2CuBr_4 [13], $Bi_{12}O_{17}Cl_2$ [14], $CuIn_5S_8$ [15], have demonstrated good photocatalytic performance for CO_2 reduction, the designed single-component photocatalysts still suffer from serious problems in the aspect of photogenerated carrier recombination, resulting in low surface charge density and difficulty in overcoming the C-C coupling energy barrier. Thus, the products of photocatalytic CO_2 reduction on the aforementioned catalysts were mainly limited to C_1 molecules (CO, CH_4, CH_3OH). More recently, a series of supported transition metal or alloy nanocatalysts have shown remarkable CO_2 reduction activity for the formation of long-chain hydrocarbons through the Fischer-Tropsch synthesis (FTS) and meantime the combination of the photothermal effect [16–18]. However, there are still rare reports on the semiconductor-based photocatalysts to transform CO_2 into C_{2+} hydrocarbon fuels driven directly by photocatalytic effect [19,20].

To tackle the carrier recombination issue, numerous approaches including morphological control [21], phase selection [22], defect engineering [23], heterojunction construction [7], and co-catalyst loading [24], have been developed so far. More specially, one of the ways for improving the surface charge density and charge transfer rate can be achieved by fabrication hybrid nanostructures via integrating the semiconductor material with a carbon material. Many carbon materials have been applied to increase the photocatalytic performance including carbon nanotube, fullerenes, carbon dots, graphene oxide, and so on [25–28]. Among these, graphdiyne (GDY), as a recently emerged carbon

---

* Corresponding author.
E-mail address: tingjiangn@163.com (T. Yan).

allotrope, has drawn huge interest in the fields of catalysis, electric devices, and solar energy conversion [29–34]. GDY is composed of both sp- and sp^2-hybridized carbon atom with two diacetylenic linkages between the adjacent carbon hexagonal structures, endowing it with excellent electrical conductivity and special geometric framework. In particular, the recent theoretical calculations and experimental results reveal that GDY also possesses outstanding hole mobility ability (1×10^4 cm^2 V^{-1} S^{-1}) and can be introduced into perovskite solar cells or photocatalytic systems for water splitting and CO_2 reduction as a hole-transfer/transporting material [35–38]. In this aspect, the favorable energy offset and tight interface in the GDY-semiconductor hybrid system can trigger fast photogenerated hole transfer from semiconductor to GDY, significantly promoting the separation of photogenerated carriers and further gathering abundant photogenerated electrons at surface active sites (such as oxygen vacancies) to reduce CO_2 into C_1 and even C_{2+} products (Scheme 1).

To the best of our knowledge, there is no work on using a GDY-semiconductor hybrid to photocatalytically transform CO_2 into C_{2+} products. Indium oxide (In_2O_3) has been widely recognized as a promising candidate for photocatalytic CO_2 reduction due to its good chemical stability, surface and optical properties, and appropriate band gap for converting CO_2 [7,8,39,40]. For example, it has been reported that In_2O_3 with engineered oxygen vacancy (electron trapping) and hydroxide (hole trapping) defects performed good photocatalytic reduction of CO_2 to CO [3,41]. Furthermore, the In_2O_3-based photocatalysts, such as Bi/In_2O_3 [7], black In_2O_3 with dense oxygen vacancy [42], $Sn-In_2O_3/In_2S_3$ [43], NiB/In_2O_3 [44], $ZnFe_2O_4/RGO/In_2O_3$ [40] have been also developed for the visible-light photocatalysis and exhibited more improvement than pristine In_2O_3. Despite In_2O_3 has the above advantages, there were also only C_1 chemicals such as CO or CH_4 in the products, no C_{2+} hydrocarbons generated in the existing photocatalysts systems. Herein, we report the synthesis of GDY-modified In_2O_3 hybrid photocatalysts (denoted as GDY-IO) via simple electrostatic attraction and thermal annealing routes. As expected, the GDY-IO composites not only deliver significantly improved photocatalytic activity in the production of CO and CH_4, but also enable the formation of C_{2+} hydrocarbons (C_2H_4, C_2H_6, C_3H_6, and C_3H_8) under atmospheric conditions. The collective experimental and theoretical results demonstrate that the introduction of GDY promotes the separation of photogenerated carriers and enhances the adsorption and activation of CO_2, and thereby significantly reduces the CH^* formation kinetics barrier and favors the hydrogenation and C-C coupling processes.
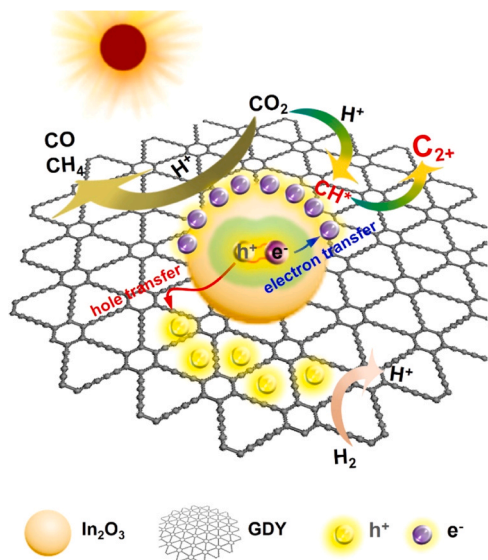
Scheme 1. The charge carrier separation pathways and photocatalytic mechanism for CO_2 hydrogenation over graphdiyne-modified In_2O_3 composite.

2. Experimental

The detailed information was shown in the Supporting information.

3. Results and discussion

3.1. Structural analysis and electron transfer

GDY-IO hybrid composites were synthesized by a two-step route (Fig. 1a). Briefly, an appropriate amount of GDY was added to the aqueous solution containing indium chloride, leading to the anchoring of indium ions on the surface of the GDY nanosheets due to the strong electrostatic attraction between In^{3+} and GDY with a negative charge [45,46]. Upon the addition of ammonium hydroxide and the subsequent oil bath treatment, the highly dispersed $GDY-In(OH)_3$ composites were synthesized by the in situ growth of $In(OH)_3$ on the surface of GDY substrate. After then, the GDY-IO hybrid composites could be achieved by a simple thermal annealing route. To confirm the formation of GDY-IO composites, we initially performed the TEM analysis on pure GDY, pristine In_2O_3 and the GDY-IO composites. As illustrated in Fig. 1b and c, GDY displays amorphous structure with thin nanosheet morphology, while the pristine In_2O_3 is primarily composed of aggregated nanocrystals with average size of 20 nm and clear lattice spacing (d = 0.293 nm) ascribing to the (222) facet of In_2O_3. As for GDY-IO composites, it is obvious that the GDY nanosheet can serve as a supporting matrix to efficiently anchor In_2O_3 nanocrystals on its surface and prevent the aggregation during the synthetic process (Fig. 1d and e). The intimate two-phase interfacial contact between highly crystallized In_2O_3 and the amorphous GDY region can effectively improve the interfacial charge transfer during the photocatalytic reaction. Furthermore, the HADDF and corresponding EDS mapping images of GDY-IO composites affirm the homogeneous distribution of In, O and C in the composites (Fig. 1f). The XRD patterns show that GDY-IO composites with different content of GDY exhibit the same crystal form as the pristine In_2O_3 (Fig. S1), characteristic of cubic phase structure (JCPDS 06–0416), indicating that the introduction of GDY does not damage the crystal structure of In_2O_3.

Raman spectroscopy is more sensitive to the carbon materials and can be applied to study the chemical structure of the composites [40]. As shown in Fig. 2a, pure GDY exhibits two major bands centered at 1597 and 1377 cm^{-1}, which can be ascribed to the typical G band and D band originating from the acetylene bonds and conjugated diyne chains, respectively [46,47]. In the case of 0.4%GDY-IO composite, some intense peaks located in the region of 100–700 cm^{-1} appear and can be attributed to the Raman-active modes of cubic phase of In_2O_3 [48]. The characteristic D and G bands assigned to GDY are also observed in 0.4% GDY-IO, confirming the presence of GDY in the composites. It should be noted that, as compared to pure GDY, the D and G bands of GDY in 0.4% GDY-IO composite display a slight shift toward lower wavenumbers, indicating a strong interaction between GDY and In_2O_3 in the composite. XPS analysis was further conducted to investigate the chemical structure and the close connections between GDY and In_2O_3. The high-resolution C 1s spectra of 0.4%GDY-IO can be deconvoluted into four peaks (Fig. 2b), which can be attributed to C=C (sp^2-hybridized carbon), C≡C (sp-hybridized carbon), C–O (epoxy or hydroxyl groups), and C=O (carboxyl or carbonyl groups), giving rise to the existence of GDY in the composites [49]. The high-resolution In 3d spectrum of In_2O_3 exhibits two peaks at 444.4 and 451.9 eV (Fig. 2c), which can be ascribed to In $3d_{5/2}$ and In $3d_{3/2}$, respectively. Notably, after coupling GDY with In_2O_3, the In 3d peaks shift to the higher binding energy compared with those of pristine In_2O_3. The same shift trend can also be observed in the O 1s spectra (Fig. 2d). These results reveal that the electron transfer occurs from In_2O_3 to GDY after contact. Moreover, the electron paramagnetic resonance (EPR) signal at the g-value of 2.003 (Fig. S2) demonstrates that the GDY-IO possessed a higher concentration of oxygen vacancies (O_v) than the pristine IO. The calculated concentration of O_v in 0.4%
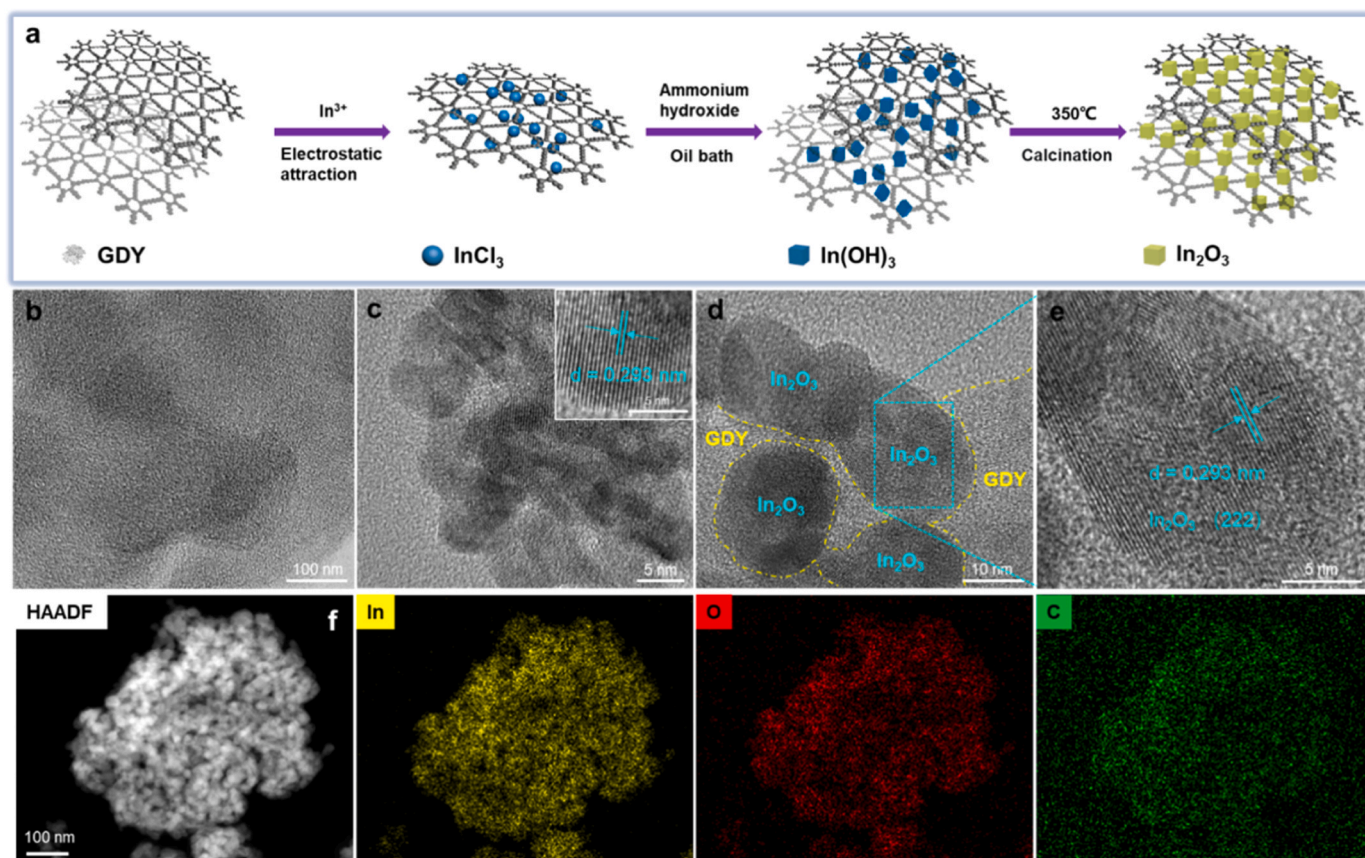
Fig. 1. (a) Schematic illustration of the synthetic process for GDY-IO composites. (b) TEM image of GDY, (c) TEM and HRTEM (insert) images of In_2O_3 nanocrystals, (d, e) TEM and HRTEM images of 0.4%GDY-IO composites, (f) HAADF and corresponding EDS mapping images of In, O and C elements in the composites.

GDY-IO and In_2O_3 from the O1s peaks in XPS further proves the conclusion (Fig. S3). Therefore, the introduction of GDY markedly increases the formation of O_v in In_2O_3, indicating the increased population of coordinately unsaturated In atoms were formed in the synthesis process. These coordinately unsaturated In atoms are electron-deficient and prone to bond with the acetylenic linkage of GDY, resulting in the strong interaction between GDY and In_2O_3.

The electron transfer at the interface of GDY-IO composites was also estimated by DFT simulation. As shown in Fig. S4, the electronic location function (ELF) demonstrates the existence of a weak covalent interaction between the C atom and the In-O layer, therefore forming a charge transfer channel and built-in electric field between IO and GDY [50]. Significantly, charge depletion and accumulation mainly occur at the GDY-IO interface (Fig. 2e). On the basis of the Mulliken population analysis (Figs. S5 and S6), it is concluded that in the composite, the C atom owes charge and the In atom gains charge, which suggests that there was a directional charge transfer from In_2O_3 to GDY layers near the interface [51]. Meanwhile, a remarkable decrease of integrated density-of-states (DOS) in the In_2O_3 after contact with GDY was observed in comparison with that before contact (Fig. 2f), implying that electron mobility is indeed accelerated from In_2O_3 to GDY.

3.2. Photocatalytic performance for CO_2 hydrogenation

The photocatalytic activity of the samples was evaluated in a batch reactor under simulated sunlight irradiation with a total reaction pressure of 0.16 MPa. The appropriate usage amount of photocatalysts in the photocatalytic reduction process was set as 5 mg (Fig. S7). In such a testing condition, the pristine In_2O_3 was found to catalyze both the reverse water gas shift (RWGS) reaction ($CO_2 + H_2 \rightarrow CO + H_2O$) and methanation reaction ($CO_2 + 4H_2 \rightarrow CH_4 + H_2O$) with CO and CH_4 as

the primary products (Fig. 3a). More surprisingly, the GDY-IO composites exhibited quite different product distribution under the same reaction conditions, namely, besides the main CO and CH_4 products, some C_{2+} hydrocarbons (C_2H_4, C_2H_6, C_3H_6, and C_3H_8) appeared in the photocatalytic process (Fig. 3a). Among these, the yields of C_2H_4 and C_2H_6 were more than C_3H_6 and C_3H_8, indicating the reduction was prone to generate C_2 products. And the amount of C_2H_6 were slightly higher than C_2H_4, indicating the higher selectivity of C_2H_6 in the C_2 products. Although the C_{2+} hydrocarbons productivity in the present study needs further research, the promotion effect of GDY on the photocatalytic synthesis of high value-added fuels shows great potential. Compared with the supported transition metal or alloy nanocatalysts that usually underwent photothermal catalytic mechanism and were highly relied on the unique plasmonic behavior, the present GDY-IO composites show negligible thermal effect since the photocatalytic performance tests are conducted under room temperature and the final bulk reaction temperature is below 120 °C. In this sense, the GDY-IO photocatalytic system is a promising material as it can transform CO_2 into C_{2+} hydrocarbon fuels driven directly by photocatalytic effect and meantime regulate the product distribution. Notably, the photocatalytic performance of GDY-IO composites was highly dependent on the content of GDY. Among the GDY-IO composites, the 0.4%GDY-IO was shown to be the optimal photocatalyst to produce both C_1 and C_{2+} products, in which the total organic carbon selectivity for C_{2+} was 14% (excluding CO).

To further explore the superiority in photocatalytic performance of 0.4%GDY-IO nanocomposite, we prepared a series of samples (0.4%GN-IO, GDY-IO mixture, and 0.4%GDY-SiO_2) as references and conducted in the same photocatalytic CO_2 hydrogenation conditions. As shown in Fig. 3a, both 0.4%GN-IO and GDY-IO mixture were active for the formation of CO and CH_4, while only 0.4%GN-IO could produce a small
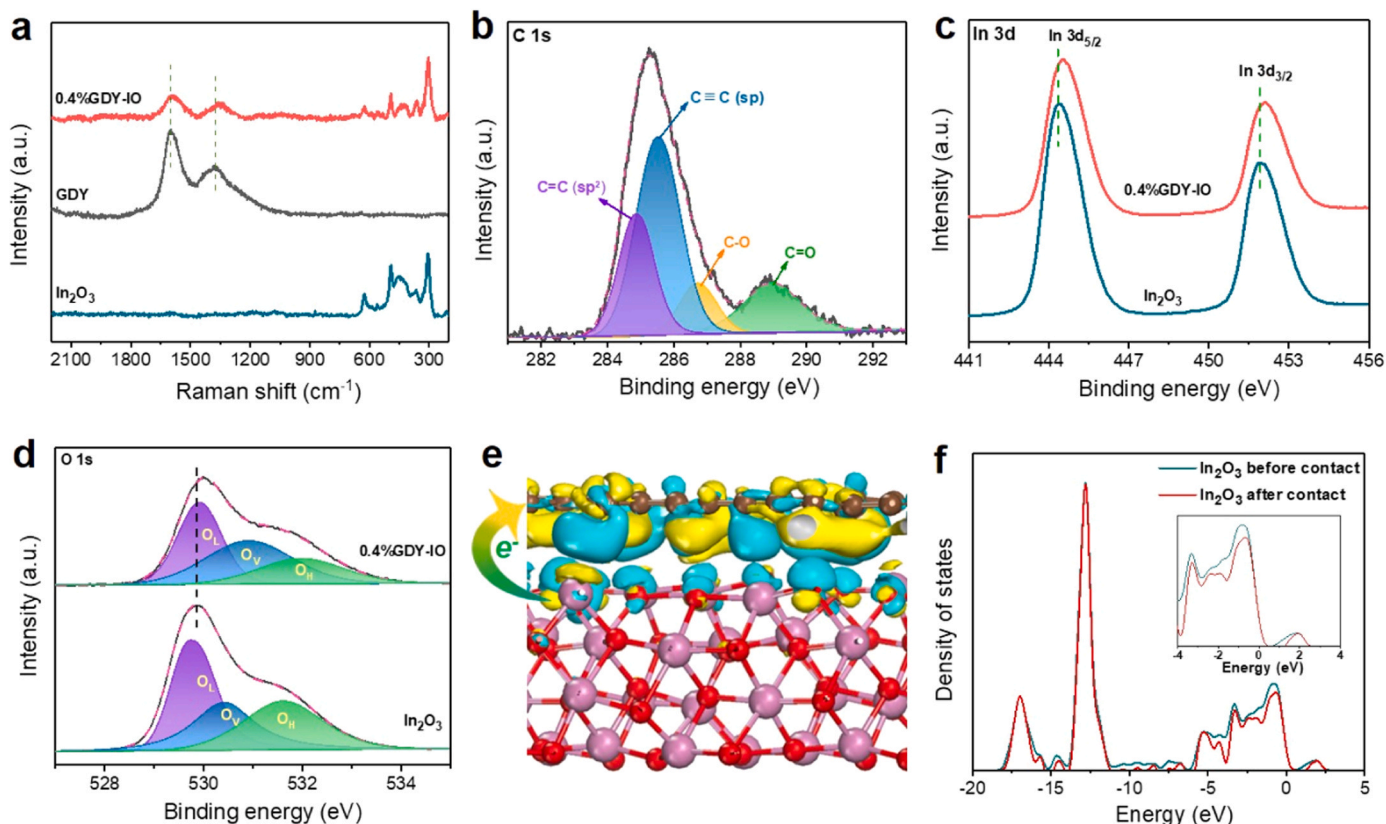
Fig. 2. (a) Raman spectra of In_2O_3, GDY and 0.4%GDY-IO composite. (b) High-resolution C 1s spectrum of 0.4%GDY-IO composite. (c) High-resolution In 3d spectra and (d) O 1s spectra of In_2O_3 and 0.4%GDY-IO composite. (e) Charge difference distribution of GDY-IO, charge accumulation is in blue and depletion in yellow. (f) Density of states of In_2O_3 before and after contact with GDY.

amount of C_{2+} hydrocarbons. As compared, all the C_1 and C_{2+} product yields for 0.4%GN-IO were much lower than that of 0.4%GDY-IO, demonstrating the superiority of GDY than graphene and the strong chemical interaction between GDY and In_2O_3. Moreover, it should be noted that no products were observed on the 0.4%GDY-SiO$_2$ sample, reflecting that In_2O_3 was also an essential factor and should be the main active component during the photocatalytic process. Using $^{13}CO_2$ isotope as the probe, the corresponding products analyzed by gas chromatography–mass spectrometry (GC-MS) confirmed the veracity of the C_{2+} hydrocarbons from CO_2 (Fig. 3b). A series of blank experiments can further support the conversion of CO_2 into carbon products (Fig. S8). Moreover, the yield of all the C_{2+} hydrocarbons maintained constant during the five consecutive runs of 20 h (Fig. 3c). The recorded XRD, TEM, and XPS of the spent 0.4%GDY-IO catalyst after 20 h of photocatalytic reaction showed no obvious structural and chemical state changes (Fig. S9), indicative of the excellent photocatalytic stability.

3.3. Mechanism for photocatalytic CO_2 hydrogenation into C_{2+} hydrocarbons

To get more insight into the origin of the production of C_{2+} hydrocarbons on GDY-IO nanocomposites, the essential ingredients involving the intrinsic electronic structure, the charge transfer mechanism and the CO_2 adsorption/activation process were considered. Upon GDY modification, the resultant GDY-IO nanocomposites exhibit an obvious light absorbance from UV to NIR region (Fig. S10), resulting in significantly enhanced efficiency of sunlight utilization. The bandgaps of the composites are calculated to be ca. 3.45 eV, much larger than that of the pristine In_2O_3 (3.11 eV). Furthermore, the band structure of GDY was also analyzed to explain the possibility of charge transfer and the enhanced photocatalytic activity. The bandgap and flat band potential

of GDY are calculated to be ca. 1.59 and 0.32 eV, respectively (Fig. 4a and b). The work function of In_2O_3 and GDY was further estimated from the energy difference of vacuum and Fermi levels according to the electrostatic potential of material by density functional theory simulation [31]. The theoretical calculation showed that In_2O_3 (110) had a lower work function than GDY (001) (4.83 vs 5.02 eV) (Fig. 4c and d). Combined the experimental and theoretical calculation results, the energy band structures of In_2O_3 and GDY were displayed in Fig. 4e. Remarkably, when In_2O_3 and GDY contacted with each other, electrons would flow from In_2O_3 to GDY to reach the same Fermi level, resulting to a built-in electric field, consistent with the above mentioned XPS and DFT results. Under light irradiation, the photogenerated holes of In_2O_3 can be driven to transfer to GDY by the built-in electric field at the composite interface, whereas the photogenerated electrons will be captured by the abundant surface oxygen vacancies of In_2O_3 (Figs. S2 and 3). As a consequence, the separation and transfer of photogenerated carries of the GDY-IO composite can be improved efficiently. Most importantly, the photogenerated electrons of In_2O_3 would migrate and aggregate at the surface oxygen vacancies, providing significantly high surface charge density to overcome the C=O activation and C-C coupling energy barrier to transform CO_2 into C_{2+} hydrocarbons.

To have an in-depth understanding on the photogenerated charge transfer mechanism, the room-temperature steady-state photoluminescence (PL) and time-resolved photoluminescence (TRPL) of pristine In_2O_3, GDY-IO and GN-IO are probed. All the three samples exhibited a broad diagnostic PL peak centered at ca. 600 nm (Fig. S11), which can be mainly attributed to the mid-gap energy levels associated with oxygen vacancies [48,52]. The existence of oxygen vacancies can be evidenced by the O 1s core level XPS and EPR spectra (Figs. 2d, S2 and 3). Obviously, the combination of GDY with In_2O_3 leads to the weakest PL emission peak, which can be due to the fact that the
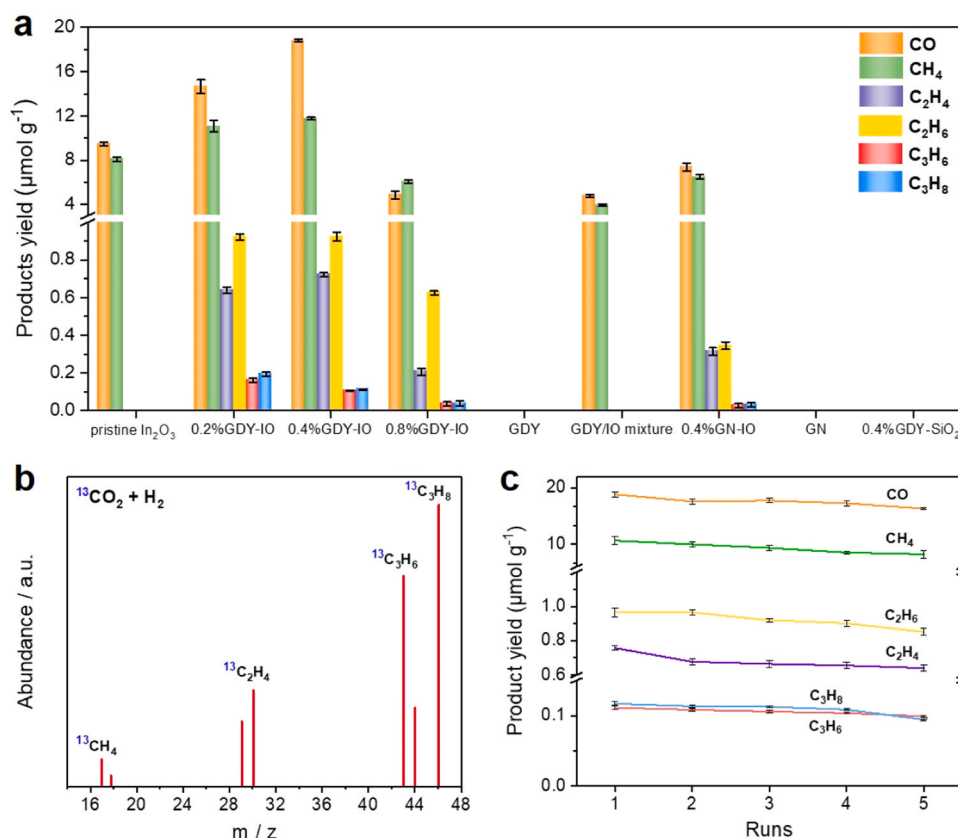
Fig. 3. (a) Products of photocatalytic CO_2 reduction on various catalysts. (b) Mass spectra of $^{13}CO_2$ isotope experiments over 0.4%GDY-IO composite. (c) Cyclic runs of products over 0.4%GDY-IO.

incorporation of GDY increased the concentration of oxygen vacancies, providing more traps capturing electrons and inhibiting the electron-hole recombination. As a result, the GDY-IO sample displayed a longer transient fluorescence lifetime (~11 ns) than pristine In_2O_3 (~5.1 ns) and GN-IO (~8.5 ns) (Fig. S12). Besides, the electrochemical characterizations including the M-S curves, transient photocurrent response and electrochemical impedance collectively indicated that the introduction of GDY is indeed capable of facilitating charge carrier separation (Figs. S13 and S14).

Apart from the electronic structure and charge transfer mechanism, the adsorption and activation of CO_2 molecules over the catalysts are also essential steps for photocatalytic CO_2 reduction. Fig. S15 illustrates the optimized models of CO_2 molecules adsorbed on In_2O_3 (110) and GDY (001) surfaces. As can be seen, the CO_2 molecule showed only physical adsorption onto In_2O_3 surface, reflecting by the constant C=O bond length and O=C=O angle. On the contrary, the linear CO_2 molecule could be highly activated by GDY to form bent chemical bonds with C atoms from the acetylenic structure. The adsorption energy of CO_2 on GDY (001) was calculated to be 0.87 eV, lower than that on In_2O_3 (110) (1.08 eV), indicating GDY was more favorable to CO_2 adsorption. The CO_2 adsorption experiments also verified that the CO_2 adsorption capacity of In_2O_3 after the introduction of GDY was enhanced (Fig. S16). Although the GDY nanosheets facilitate the dispersion of the In_2O_3 nanoparticles, contributing to increased surface areas for GDY-IO nanocomposites (Fig. S17 and Table S1), the physical adsorption of CO_2 should not be the critical factor in boosting the photocatalytic performance. The effect of GDY introduction on the chemical interaction between CO_2 and catalysts was further investigated by CO_2 temperature-programmed desorption (CO_2-TPD) measurements. As shown in Fig. S18, two weak and broad desorption peaks at around 125 and 275 °C were observed for both GDY-IO and In_2O_3. These two desorption peaks can be attributed to the physically adsorbed CO_2 and

the chemical bonding of CO_2 with oxygen vacancies, respectively [53]. Obviously, the intensity of these two peaks for 0.4%GDY-IO nanocomposite is a slightly higher than that of pristine In_2O_3. This can be well explained by the increased surface areas and the higher concentration of oxygen vacancies after GDY modification. Moreover, significant desorption peaks at higher temperatures (300–700 °C) were clearly observed for the two samples and can be related to the decomposition of HCO_3^- and CO_3^{2-} intermediate species [8,54]. Of note, the intensity of these species over 0.4%GDY-IO nanocomposite was much lower than those on pristine In_2O_3, implying that the HCO_3^- and CO_3^{2-} intermediates formed on GDY-IO were easier to desorb and thereby transformed into the C_{2+} hydrocarbons.

The surface species formed on GDY-IO and In_2O_3 were further identified by the in situ diffuse reflectance infrared Fourier-transform spectroscopy (in situ DRIFTs). Fig. 5a shows the transient evolution of the surface species over GDY-IO in a flow cell under reaction operando conditions. Two primary surface species were detected during the light irradiation period (0–40 min). The first kind of species signaled by fingerprint modes in the region of 1400–1800 cm^{-1} could be assigned to the chemisorbed CO_2 species including carbonate (CO_3^{2-}) and bicarbonate (HCO_3^-) [4,8,55–57]. The second kind of species with fingerprint modes at 1065, 3240, 2876 cm^{-1} were attributed to the vibrations of C–H, =CH– and –CH_2– groups from the multi-carbon products [58]. Note that, along with the photocatalytic CO_2 hydrogenation, the bands of the carbonate and bicarbonate species gradually decreased and disappeared, accompanied with the gradual increase of the intensity for the =CH– and –CH_2– groups, strongly supporting the transformation of carbonate and bicarbonate intermediate species into the C_{2+} hydrocarbon products, well consistent with the CO_2-TPD results. The intermediates of the reaction process on In_2O_3 can be also observed in DRIFTs spectra as shown in the Fig. S19. However, compared with the signals of all these species over GDY-IO, they were much weaker under
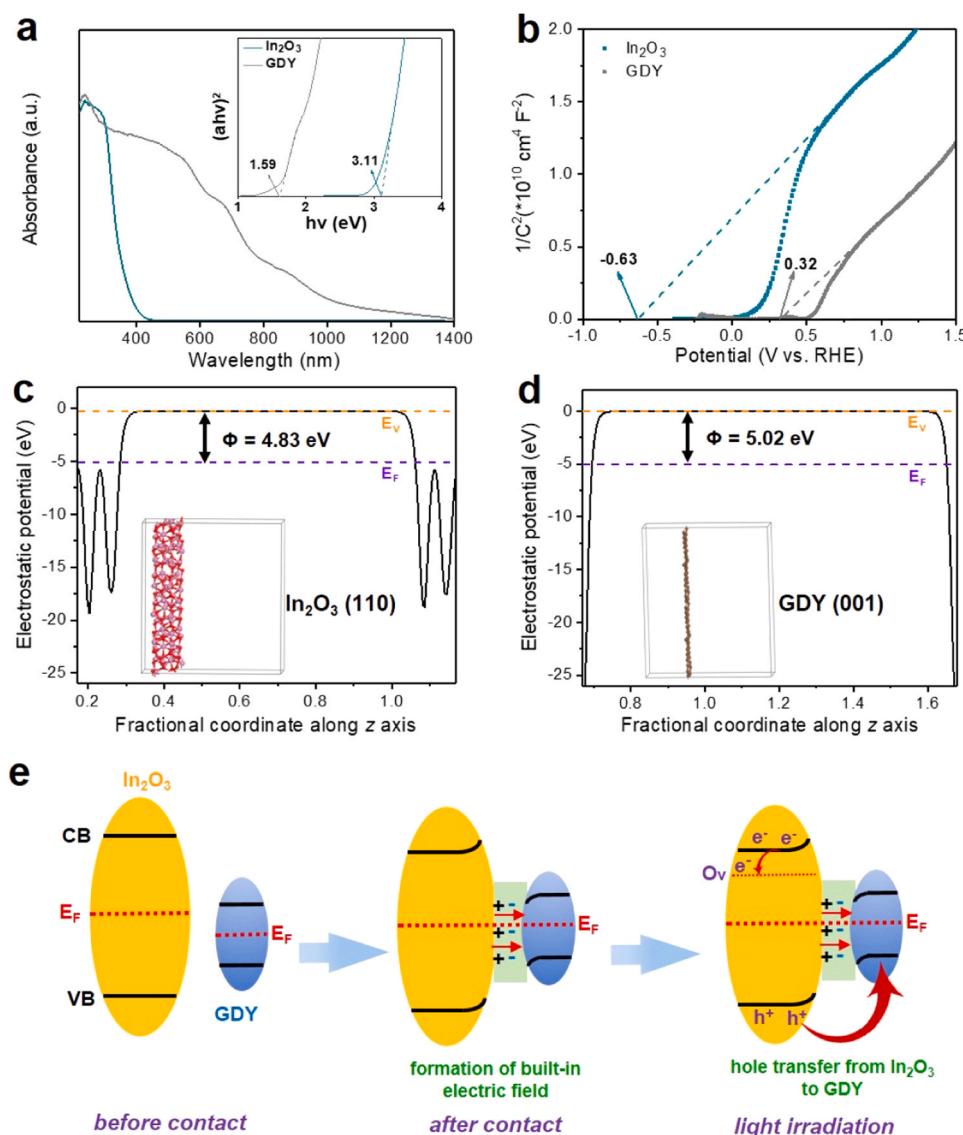
Fig. 4. (a) Bandgap values and (b) Mott–Schottky plots of In_2O_3 and GDY. Calculated electrostatic potentials for (c) In_2O_3 (110) face and (d) GDY (001) face. (e) Schematic diagram for the electron transfer and the formation of built-in electric field between In_2O_3 and GDY upon their contact, and the holes transfer between In_2O_3 and GDY after light irradiation.

the same light irradiation period (Fig. 5b), in accordance with the photocatalytic performance.

To further understand the favorable effect of GDY modification on the generation of C_{2+} hydrocarbons especially C_2H_4 and C_2H_6, the free energy changes during the CO_2 hydrogenation reaction were performed on GDY-IO and pristine In_2O_3. It is generally accepted that the formation of C_{2+} hydrocarbons usually involves the activation of CO_2 to CO* through COOH* intermediate and the subsequent hydrogenation and coupling of CH* [58,59]. As shown in Fig. 5c, the rate-limiting step of the CO_2 hydrogenation on In_2O_3 was the conversion of HOCH* to CH* (Fig. 5c, Sections VI and VII), with the protonation kinetics barrier being 1.52 eV (derived from 3.46 to 1.94). As compared, the rate-limiting step of the CO_2 hydrogenation on GDY-IO was the conversion of CO_2* to COOH* (Fig. 5d, Sections II and III), with the protonation kinetics barrier being 0.56 eV (derived from 1.05 to 0.49). The energy barrier for the reaction on In_2O_3 is much higher than that on GDY-IO, evidencing that the introduction of GDY significantly facilitates the CO_2 hydrogenation. In_2O_3 is prone to hydrogenation of CO*, whereas the HOCH* protonation kinetics barrier is significantly higher at 3.46 eV. However, for GDY-IO, the HOCH* protonation kinetics barrier is significantly lower at

1.15 eV, availing the further transformation to CH*. Moreover, the reaction path for CO_2 reduction on the pristine GDY was also calculated (Fig. S20). The protonation kinetics barrier of the conversion of CO_2* to COOH* on GDY was higher (0.75 eV) than that on In_2O_3 (0.04 eV), indicating GDY did not avail the generation of COOH* intermediates. Furthermore, the rate-limiting step of the CO_2 hydrogenation on GDY was also the conversion of HOCH* to CH*, with the protonation kinetics barrier being achieved to 1.95 eV, indicating CH* was not easily generated on GDY. Therefore, the introduction of GDY facilitates the CO_2 adsorption and activation, and In_2O_3 played a catalytic role in the reduction of CO_2 on GDY-IO composite. GDY-IO interface may stabilize the key HOCH* intermediate and significantly reduce the kinetics barrier to avail CH* formation, tuning the subsequent hydrogenation and C-C coupling into thermodynamically favorable exothermal processes. In the following steps, the hydrogenations of CH* to produce CH_2* are thermodynamically favorable with 0.73 eV of energy emission. The formation of CH_3* and C_2H_4* intermediates release 0.68 and 1.34 eV of energy from CH_2*, respectively, indicating that the formation of CH_3* and C_2H_4* are both spontaneous processes. The C–C coupling between CH_3* and CH_3*, or the further hydrogenation of C_2H_4*, is considered a
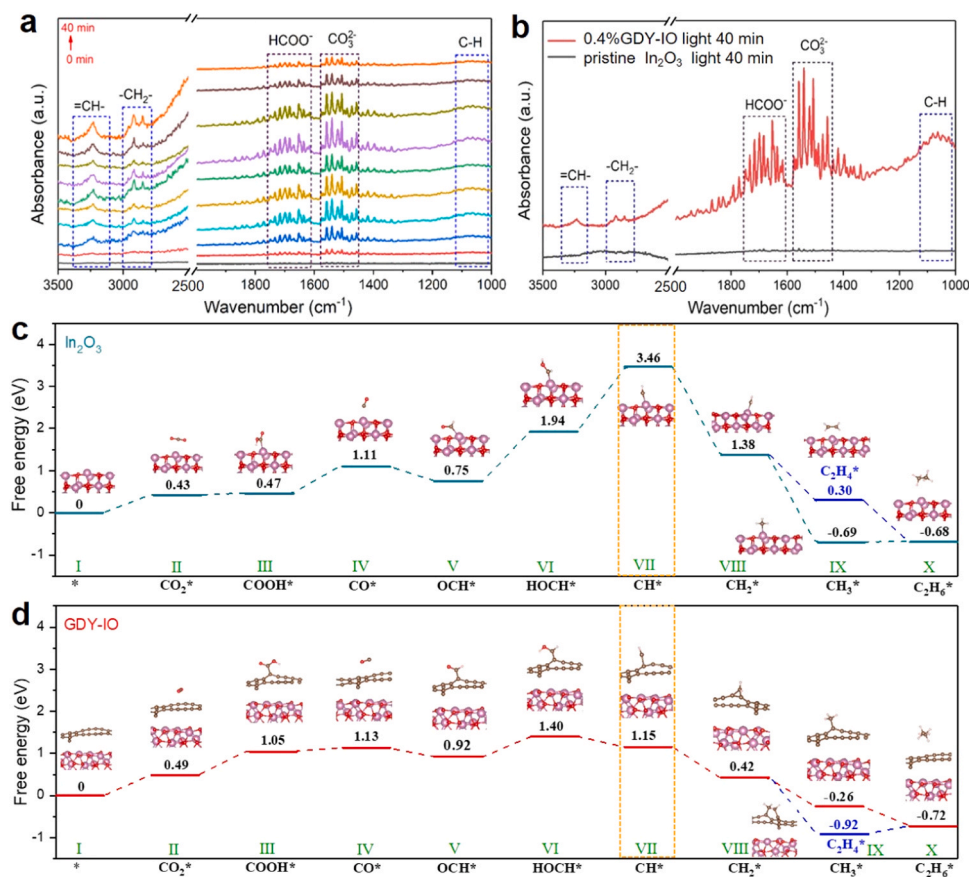
Fig. 5. (a) *In situ* DRIFTs during the photocatalytic process on 0.4%GDY-IO composite under light irradiation conditions. (b) Comparison of in situ DRIFTs spectra of 0.4%GDY-IO composite and pristine In_2O_3 under light irradiation condition. Computed Gibbs free energy for main reactions in photocatalytic reduction of CO_2 on (c) pristine In_2O_3 and (d) GDY-IO composite.

critical step in the generation of C_2H_6. Therefore, the evolution process of $CH^* \rightarrow CH_2^* \rightarrow CH_3^*$(or $C_2H_4^*$) $\rightarrow C_2H_6^*$ (Sections from VII to X) is exothermal and beneficial for C_{2+} hydrocarbons, such as C_2H_4 and C_2H_6, which is absolutely consistent with the catalytic results (Fig. 3a). The collective in situ DRIFTs and DFT results demonstrate that the introduction of GDY into In_2O_3 can enhance the adsorption and activation of CO_2, and cause the electron enrichment on the In_2O_3 surfaces near the oxygen vacancies, which together benefit for stabilizing the reaction intermediates and promote the C-C coupling reactions.

4. Conclusions

In summary, graphdiyne/In_2O_3 (GDY-IO) nanocomposites were firstly synthesized and applied in the gas phase photocatalytic reduction of CO_2 to C_{2+} hydrocarbons. By adjusting the composite ratio of GDY and In_2O_3, the 0.4%GDY-IO catalyst exhibited the optimal C_{2+} hydrocarbons production activity and a high selectivity of 14% under simulated solar light irradiation and atmospheric pressure. The collective experimental and theoretical results indicated that the introduced GDY in the GDY-IO composite can function as excellent hole-transfer/transporting media, good light absorber, and proper CO_2 active sites, which consequently enhance the absorption of sunlight, promote CO_2 activation and improve the separation efficiency of photogenerated carriers. Meantime, the lower energy barrier of CH* intermediates formation and sufficient electrons accumulated on the surface of the composite availed for hydrogenation and subsequent coupling reactions. This work developed a GDY-based composite catalyst for harnessing solar-energy to synthesize high value-added hydrocarbons products towards selective CO_2 conversion in energy conversion field.

CRediT authorship contribution statement

Wenjuan Li: Conceptualization, Methodology, Visualization, Writing – review & editing. **Yipin Zhang:** Methodology, Data curation. **Yuhua Wang:** Software, Methodology, Data curation. **Weiguang Ran:** Software, Methodology, Data curation. **Qinhui Guan:** Methodology. **Wencai Yi:** Methodology. **Lulu Zhang:** Formal analysis. **Dapeng Zhang:** Formal analysis. **Na Li:** Formal analysis. **Tingjiang Yan:** Supervision, Conceptualization, Methodology, Visualization, Writing – review & editing.

Declaration of Competing Interest

The authors declare that they have no known competing financial interests or personal relationships that could have appeared to influence the work reported in this paper.

Data availability

The data that has been used is confidential.

Appendix A. Supporting information

Supplementary data associated with this article can be found in the online version at doi:10.1016/j.apcatb.2023.123267.

References

[1] L. Al-Ghussain, Global warming: review on driving forces and mitigation, Environ. Prog. Sustain. 38 (2019) 13–21.

[2] S.I. Zandalinas, F.B. Fritschi, R. Mittler, Global warming, climate change, and environmental pollution: recipe for a multifactorial stress combination disaster, Trends Plant Sci. 26 (2021) 588–599.

[3] L.B. Hoch, T.E. Wood, P.G. O'Brien, K. Liao, L.M. Reyes, C.A. Mims, G.A. Ozin, The rational design of a single-component photocatalyst for gas-phase CO_2 reduction using both UV and visible light, Adv. Sci. 1 (2014).

[4] J. Di, C. Chen, C. Zhu, P. Song, J. Xiong, M. Ji, J. Zhou, Q. Fu, M. Xu, W. Hao, J. Xia, S. Li, H. Li, Z. Liu, Bismuth vacancy-tuned bismuth oxybromide ultrathin nanosheets toward photocatalytic CO_2 reduction, ACS Appl. Mater. Interfaces 11 (2019) 30786–30792.

[5] L. Wang, G. Liu, B. Wang, X. Chen, C. Wang, Z. Lin, J. Xia, H. Li, Oxygen vacancies engineering–mediated BiOBr atomic layers for boosting visible light-driven photocatalytic CO_2 reduction, Sol. RRL 5 (2021) 2000480.

[6] Q. Wang, Z. Miao, Y. Zhang, T. Yan, L. Meng, X. Wang, Photocatalytic reduction of CO_2 with H_2O mediated by Ce-tailored bismuth oxybromide surface frustrated Lewis pairs, ACS Catal. 12 (2022) 4016–4025.

[7] T. Yan, N. Li, L. Wang, Q. Liu, A. Jelle, L. Wang, Y. Xu, Y. Liang, Y. Dai, B. Huang, J. You, G.A. Ozin, How to make an efficient gas-phase heterogeneous CO_2 hydrogenation photocatalyst, Energy Environ. Sci. 13 (2020) 3054–3063.

[8] T. Yan, N. Li, L. Wang, W. Ran, P.N. Duchesne, L. Wan, N. Nhat Truong, L. Wang, M. Xia, G.A. Ozin, Bismuth atom tailoring of indium oxide surface frustrated Lewis pairs boosts heterogeneous CO_2 photocatalytic hydrogenation, Nat. Commun. 11 (2020) 6095.

[9] T.T. Kong, Y.W. Jiang, Y.J. Xiong, Photocatalytic CO_2 conversion: what can we learn from conventional CO_x hydrogenation? Chem. Soc. Rev. 49 (2020) 6579–6591.

[10] E.V. Kondratenko, G. Mul, J. Baltrusaitis, G.O. Larrazábal, J. Pérez-Ramírez, Status and perspectives of CO_2 conversion into fuels and chemicals by catalytic, photocatalytic and electrocatalytic processes, Energy Environ. Sci. 6 (2013) 3112–3135.

[11] S.N. Habisreutinger, L. Schmidt-Mende, J.K. Stolarczyk, Photocatalytic reduction of CO_2 on TiO_2 and other semiconductors, Angew. Chem. Int. Ed. 52 (2013) 7372–7408.

[12] W. Zhong, R. Sa, L. Li, Y. He, L. Li, J. Bi, Z. Zhuang, Y. Yu, Z. Zou, A covalent organic framework bearing single Ni sites as a synergistic photocatalyst for selective photoreduction of CO_2 to CO, J. Am. Chem. Soc. 141 (2019) 7615–7621.

[13] J. Sheng, Y. He, M. Huang, C. Yuan, S. Wang, F. Dong, Frustrated Lewis pair sites boosting CO_2 photoreduction on Cs_2CuBr_4 perovskite quantum dots, ACS Catal. 12 (2022) 2915–2926.

[14] J. Di, C. Zhu, M. Ji, M. Duan, R. Long, C. Yan, K. Gu, J. Xiong, Y. She, J. Xia, H. Li, Z. Liu, Defect-rich $Bi_{12}O_{17}Cl_2$ nanotubes self-accelerating charge separation for boosting photocatalytic CO_2 reduction, Angew. Chem. Int. Ed. 57 (2018) 14847–14851.

[15] X. Li, Y. Sun, J. Xu, Y. Shao, J. Wu, X. Xu, Y. Pan, H. Ju, J. Zhu, Y. Xie, Selective visible-light-driven photocatalytic CO_2 reduction to CH_4 mediated by atomically thin $CuIn_5S_8$ layers, Nat. Energy 4 (2019) 690–699.

[16] Z. Li, J. Liu, Y. Zhao, R. Shi, G.I.N. Waterhouse, Y. Wang, L. Wu, C. Tung, T. Zhang, Photothermal hydrocarbon synthesis using alumina-supported cobalt metal nanoparticle catalysts derived from layered-double-hydroxide nanosheets, Nano Energy 60 (2019) 467–475.

[17] G. Chen, R. Gao, Y. Zhao, Z. Li, G.I.N. Waterhouse, R. Shi, J. Zhao, M. Zhang, L. Shang, G. Sheng, X. Zhang, X. Wen, L.Z. Wu, C.H. Tung, T. Zhang, Alumina-supported CoFe alloy catalysts derived from layered-double-hydroxide nanosheets for efficient photothermal CO_2 hydrogenation to hydrocarbons, Adv. Mater. 30 (2018) 1704663.

[18] Y. Wang, Y. Zhao, J. Liu, Z. Li, G.I.N. Waterhouse, R. Shi, X. Wen, T. Zhang, Manganese oxide modified nickel catalysts for photothermal CO hydrogenation to light olefins, Adv. Energy Mater. 10 (2019) 1902860.

[19] Y. Shen, Y. Ren, L. Zheng, X. Xu, R. Long, W. Zhang, Y. Yang, Y. Zhang, Y. Yao, H. Chi, J. Wang, Q. Shen, Y. Xiong, Z. Zou, Y. Zhou, Room-temperature photosynthesis of propane from CO_2 with Cu single atoms on vacancy-rich TiO_2, Nat. Commun. 14 (2023) 1117.

[20] C. Lv, X. Bai, S. Ning, C. Song, Q. Guan, B. Liu, Y. Li, J. Ye, Nanostructured materials for photothermal carbon dioxide hydrogenation: regulating solar utilization and catalytic performance, ACS Nano 17 (2023) 1725–1738.

[21] Z. Liu, H. Yang, J. Wang, Y. Yuan, K. Hills-Kimball, T. Cai, P. Wang, A. Tang, O. Chen, Synthesis of lead-free Cs_2AgBiX_6 (X = Cl, Br, I) double perovskite nanoplatelets and their application in CO_2 photocatalytic reduction, Nano Lett. 21 (2021) 1620–1627.

[22] T. Yan, L. Wang, Y. Liang, M. Makaremi, T.E. Wood, Y. Dai, B. Huang, A.A. Jelle, Y. Dong, G.A. Ozin, Polymorph selection towards photocatalytic gaseous CO_2 hydrogenation, Nat. Commun. 10 (2019) 2521.

[23] S. Bai, N. Zhang, C. Gao, Y. Xiong, Defect engineering in photocatalytic materials, Nano Energy 53 (2018) 296–336.

[24] Y. Pan, Y. Qian, X. Zheng, S. Chu, Y. Yang, C. Ding, X. Wang, S. Yu, H. Jiang, Precise fabrication of single-atom alloy co-catalyst with optimal charge state for enhanced photocatalysis, Natl. Sci. Rev. 8 (2021) 224.

[25] K. Woan, G. Pyrgiotakis, W. Sigmund, Photocatalytic carbon-nanotube–TiO_2 composites, Adv. Mater. 21 (2009) 2233–2239.

[26] A. Kongkanand, P.V. Kamat, Electron storage in single wall carbon nanotubes. Fermi level equilibration in semiconductor–SWCNT suspensions, ACS Nano 1 (2007) 13–21.

[27] J. Du, X. Lai, N. Yang, J. Zhai, D. Kisailus, F. Su, D. Wang, L. Jiang, Hierarchically ordered macro−mesoporous TiO_2−graphene composite films: improved mass transfer, reduced charge recombination, and their enhanced photocatalytic activities, ACS Nano 5 (2011) 590–596.

[28] Y. Pan, Y. You, S. Xin, Y. Li, G. Fu, Z. Cui, Y. Men, F. Cao, S. Yu, J.B. Goodenough, Photocatalytic CO_2 reduction by carbon-coated indium-oxide nanobelts, J. Am. Chem. Soc. 139 (2017) 4123–4129.

[29] S. Wang, L. Yi, J.E. Halpert, X. Lai, Y. Liu, H. Cao, R. Yu, D. Wang, Y. Li, A novel and highly efficient photocatalyst based on P25–graphdiyne nanocomposite, Small 8 (2012) 265–271.

[30] S. Thangavel, K. Krishnamoorthy, V. Krishnaswamy, N. Raju, S.J. Kim, G. Venugopal, Graphdiyne–ZnO nanohybrids as an advanced photocatalytic material, J. Phys. Chem. C 119 (2015) 22057–22065.

[31] F.Y. Xu, K. Meng, B.C. Zhu, H.B. Liu, J.S. Xu, J.G. Yu, Graphdiyne: a new photocatalytic CO_2 reduction cocatalyst, Adv. Funct. Mater. 29 (2019) 1904256.

[32] K. Su, G. Dong, W. Zhang, Z. Liu, M. Zhang, T. Lu, In situ coating $CsPbBr_3$ nanocrystals with graphdiyne to boost the activity and stability of photocatalytic CO_2 reduction, ACS Appl. Mater. Interfaces 12 (2020) 50464–50471.

[33] Q. Xu, B. Zhu, B. Cheng, J. Yu, M. Zhou, W. Ho, Photocatalytic H_2 evolution on graphdiyne/g-C_3N_4 hybrid nanocomposites, Appl. Catal. B Environ. 255 (2019), 117770.

[34] Y. Fang, Y. Xue, L. Hui, H. Yu, Y. Li, Graphdiyne@Janus magnetite for photocatalytic nitrogen fixation, Angew. Chem. Int. Ed. 60 (2021) 3170.

[35] M. Long, L. Tang, D. Wang, Y. Li, Z. Shuai, Electronic structure and carrier mobility in graphdiyne sheet and nanoribbons: theoretical predictions, ACS Nano 5 (2011) 2593–2600.

[36] J. Lv, Z. Zhang, J. Wang, X. Lu, W. Zhang, T. Lu, In situ synthesis of CdS/graphdiyne heterojunction for enhanced photocatalytic activity of hydrogen production, ACS Appl. Mater. Interfaces 11 (2019) 2655–2661.

[37] C. Sun, Y. Liu, Z. Wang, P. Wang, Z. Zheng, H. Cheng, X. Qin, X. Zhang, Y. Dai, B. Huang, Self-assembled g-C_3N_4 nanotubes/graphdiyne composite with enhanced photocatalytic CO_2 reduction, J. Alloy. Compd. 868 (2021), 159045.

[38] J. Li, L. Zhu, C. Tung, L. Wu, Engineering graphdiyne for solar photocatalysis, Angew. Chem. Int. Ed. (2023) 202301384.

[39] L. Wang, M. Ghoussoub, H. Wang, Y. Shao, W. Sun, A.A. Tountas, T.E. Wood, H. Li, J.Y.Y. Loh, Y. Dong, M. Xia, Y. Li, S. Wang, J. Jia, C. Qiu, C. Qian, N.P. Kherani, L. He, X. Zhang, G.A. Ozin, Photocatalytic hydrogenation of carbon dioxide with high selectivity to methanol at atmospheric pressure, Joule 2 (2018) 1369–1381.

[40] J. Li, F. Wei, C. Dong, W. Mu, X. Han, A Z-scheme $ZnFe_2O_4$/RGO/In_2O_3 hierarchical photocatalyst for efficient CO_2 reduction enhancement, J. Mater. Chem. A 8 (2020) 6524–6531.

[41] J.Y. Wang, G.H. Zhang, J. Zhu, X.B. Zhang, F.S. Ding, A.F. Zhang, X.W. Guo, C.S. Song, CO_2 hydrogenation to methanol over In_2O_3-based catalysts: from mechanism to catalyst development, ACS Catal. 11 (2021) 1406–1423.

[42] L. Wang, Y. Dong, T. Yan, Z. Hu, A.A. Jelle, D.M. Meira, P.N. Duchesne, J.Y.Y. Loh, C. Qiu, E.E. Storey, Y. Xu, W. Sun, M. Ghoussoub, N.P. Kherani, A.S. Helmy, G.A. Ozin, Black indium oxide a photothermal CO_2 hydrogenation catalyst, Nat. Commun. 11 (2020) 2432.

[43] Y. Ma, Z. Zhang, X. Jiang, R. Sun, M. Xie, W. Han, Direct Z-scheme Sn-In_2O_3/In_2S_3 heterojunction nanostructures for enhanced photocatalytic CO_2 reduction activity, J. Mater. Chem. C 9 (2021) 3987–3997.

[44] J. He, P. Lyu, B. Jiang, S. Chang, H. Du, J. Zhu, H. Li, A novel amorphous alloy photocatalyst (NiB/In_2O_3) composite for sunlight-induced CO_2 hydrogenation to HCOOH, Appl. Catal. B Environ. 298 (2021), 120603.

[45] J. Zhao, Z. Xiong, Y. Zhao, J. Wang, Y. Qiu, P. Liu, J. Zhang, 2D/2D heterostructure of metal-free ultrathin graphdiyne/carbon nitride nanosheets for enhanced photocatalytic reduction of carbon dioxide with water, ACS Appl. Energy Mater. 4 (2021) 12403–12410.

[46] C. Yang, Y. Wang, J. Yu, S. Cao, Ultrathin 2D/2D graphdiyne/Bi_2WO_6 heterojunction for gas-phase CO_2 photoreduction, ACS Appl. Energy Mater. 4 (2021) 8734–8738.

[47] G. Li, Y. Li, H. Liu, Y. Guo, Y. Li, D. Zhu, Architecture of graphdiyne nanoscale films, Chem. Commun. 46 (2010) 3256.

[48] K. Yadav, B.R. Mehta, J.P. Singh, Template-free synthesis of vertically aligned crystalline indium oxide nanotube arrays by pulsed argon flow in a tube-in-tube chemical vapor deposition system, J. Mater. Chem. C 2 (2014) 6362–6369.

[49] S. Cao, Y. Wang, B. Zhu, G. Xie, J. Yu, J. Gong, Enhanced photochemical CO_2 reduction in the gas phase by graphdiyne, J. Mater. Chem. A 8 (2020) 7671–7676.

[50] H. Wang, Y. Sun, G. Jiang, Y. Zhang, H. Huang, Z. Wu, S.C. Lee, F. Dong, Unraveling the mechanisms of visible light photocatalytic NO purification on earth-abundant insulator-based core−shell heterojunctions, Environ. Sci. Technol. 52 (2018) 1479–1487.

[51] W. Dai, Z. Zhao, Understanding the interfacial properties of graphene-based materials/BiOI heterostructures by DFT calculations, Appl. Surf. Sci. 406 (2017) 8–20.

[52] K. Yadav, B.R. Mehta, K.V. Lakshmi, S. Bhattacharya, J.P. Singh, Tuning the wettability of indium oxide nanowires from superhydrophobic to nearly

superhydrophilic: effect of oxygen-related defects, J. Phys. Chem. C 119 (2015) 16026–16032.

[53] S.W. Li, Y. Xu, Y.F. Chen, W.Z. Li, L.L. Lin, M.Z. Li, Y.C. Deng, X.P. Wang, B.H. Ge, C. Yang, S.Y. Yao, J.L. Xie, Y.W. Li, X. Liu, D. Ma, Tuning the selectivity of catalytic carbon dioxide hydrogenation over iridium/cerium oxide catalysts with a strong metal–support interaction, Angew. Chem. Int. Ed. 56 (2017) 10761–10765.

[54] C. Luo, J. Zhao, Y.X. Li, W. Zhao, Y.B. Zeng, C.Y. Wang, Photocatalytic CO_2 reduction over $SrTiO_3$: correlation between surface structure and activity, Appl. Surf. Sci. 447 (2018) 627–635.

[55] F. Wang, T. Hou, X. Zhao, W. Yao, R. Fang, K. Shen, Y. Li, Ordered macroporous carbonous frameworks implanted with CdS quantum dots for efficient photocatalytic CO_2 reduction, Adv. Mater. 33 (2021) 2102690.

[56] M. Xu, X. Zhao, H. Jiang, S. Chen, P. Huo, MOFs-derived $C-In_2O_3/g-C_3N_4$ heterojunction for enhanced photoreduction CO_2, J. Environ. Chem. Eng. 9 (2021), 106469.

[57] Y. Shen, Q. Han, J. Hu, W. Gao, L. Wang, L. Yang, C. Gao, Q. Shen, C. Wu, X. Wang, X. Zhou, Y. Zhou, Z. Zou, Artificial trees for artificial photosynthesis: construction of dendrite-structured $\alpha-Fe_2O_3/g-C_3N_4$ Z-scheme system for efficient CO_2 reduction into solar fuels, ACS Appl. Energy Mater. 3 (2020) 6561–6572.

[58] L. Wang, B. Zhao, C. Wang, M. Sun, Y. Yu, B. Zhang, Thermally assisted photocatalytic conversion of $CO_2–H_2O$ to C_2H_4 over carbon doped In_2S_3 nanosheets, J. Mater. Chem. A 8 (2020) 10175–10179.

[59] H. Ou, G. Li, W. Ren, B. Pan, G. Luo, Z. Hu, D. Wang, Y. Li, Atomically dispersed Au-assisted $C–C$ coupling on red phosphorus for CO_2 photoreduction to C_2H_6, J. Am. Chem. Soc. 144 (2022) 22075–22082.